Multidimensional Simulation of Plasma in Argon through a Shock in Hypersonic Flow

Amrita K. Lonkar*, Francisco Palacios†
Robert W. MacCormack‡, and Juan J. Alonso§
Stanford University, Stanford, CA 94305, U.S.A.

We present a new numerical formulation governing the physics of a plasma near strong shock waves in gases at hypersonic speeds. A plasma is composed of multiple species in thermo-chemical nonequlibrium, thus making high-fidelity numerical modeling challenging. In order to reduce the size and complexity of the problem, a number of simulation approaches take advantage of simplifications concerning the flow properties of the various species. The plasma is also often assumed to be charge neutral in order to bypass the requirement of the solution of Maxwell's equations. In this work, we drop these simplifications and solve the full Navier-Stokes equations for each species in the plasma including the physics of thermo-chemical nonequilibrium, along with Maxwell's equations to account for electrodynamic effects. The full set of equations has been programmed in the "Stanford University Unstructured" (SU^2) open source suite of tools, and two different test cases have been simulated and compared with published data. In the first case, the unsteady dynamics of plasma formation near a normal shock wave at Mach 15 are modeled and compared with previous work. In the second case, heat transfer to a three dimensional body from a stream of plasma at Mach 4.6 is simulated and compared with experimental data. The two test cases show an excellent match with published data. In addition to this validation / verification study, this paper also presents the formulation and numerical implementation of our model for the equations governing high-temperature plasmas.

Nomenclature

Subscripts

s	Species
e^-	Electron gas
n	Argon gas
i	Argon ion gas

Variable Names

ρ	Mass density
ρ_c	Charge density
$\vec{v}$	Fluid velocity
u_{s_j}	Component of velocity of species s in direction j
E	Total energy per unit mass

*Ph.D. Candidate, Department of Aeronautics & Astronautics, AIAA Student Member.
†Engineering Research Associate, Department of Aeronautics & Astronautics, AIAA Member.
‡Professor, Department of Aeronautics & Astronautics, AIAA Fellow.
§Associate Professor, Department of Aeronautics & Astronautics, AIAA Senior Member.

P	Partial pressure
T	Temperature
ϕ	Electrostatic potential
$\vec{E}$	Electric field
$\vec{B}$	Magnetic field
$E_{mf_{s_k}}$	Component of electromagnetic force on species s in k direction
σ_e	Electrical conductivity
k_{f_s}	Rate constant of forward reaction of species s
k_{b_s}	Rate constant of backward reaction of species s
k_{e_s}	Rate constant of equilibrium of species s
R	Rate of reaction

Gas Properties

M	Molecular weight
m	Mass of one particle
C_v	Specific heat capacity calculated at constant volume
γ	Ratio of specific heats
ϵ_0	Electric permittivity
μ_0	Magnetic permeability
N_A	Avogadro's number
e_c	Electric charge

Mathematical Notation

$\vec{a}$	Spatial vector $a \in \mathbb{R}^n$, where n is the dimension of the physical cartesian space (in general, 2 or 3)
$\vec{A}$	(A_x, A_y) in two dimensions or (A_x, A_y, A_z) in three dimensions, where A_k is a column vector
$\nabla(\cdot)$	Spatial gradient operator
$\nabla \cdot (\cdot)$	Spatial divergence operator
$\partial_n(\cdot)$	Normal gradient operator at a surface point, $\vec{n}_S \cdot \nabla(\cdot)$
$\nabla_S(\cdot)$	Tangential gradient operator at a surface point, $\nabla(\cdot) - \partial_n(\cdot)$
$\cdot$	Spatial inner product
$\times$	Spatial cross product

1. Introduction

THERE have been major advancements in the field of hypersonics in the past quarter century. Rocket-powered launch vehicles typically achieve hypersonic speeds in the upper atmosphere while transporting payloads to orbit. Shuttles carrying humans re-enter the Earth's atmosphere at hypersonic speeds. To reduce uncertainties and increase safety in these extraordinary accomplishments, it is important to fully understand the dynamics of flow at such high speeds and rarified atmospheres.

Flows past vehicle configurations at hypersonic speeds undergo a change in state from a gaseous form to a state of plasma at the location of strong shock waves. When a gas moving at high Mach numbers encounters a shock wave, there is a strong discontinuity in the fluid properties which results in intense heating of the gas to very high temperatures right behind the shock wave. Heat causes some molecules in the gas to ionize into ions and free electrons which exert strong electromagnetic forces on one another. These electromagnetic forces impart this quasi-neutral mixture of gases a *collective*[1] behavior: a property of plasmas not exhibited by gases.

In order to fully understand the behavior of high-enthalpy flows around hypersonic vehicles, it is important to understand the physics of plasma formation. Numerical modeling of plasmas is considerably more complex than that of gas flows. This is partly because there are multiple species present in a plasma which exhibit a collective behavior and partly because these species are in thermo-chemical nonequlibrium. Therefore

a full description of the properties of a plasma requires the solution at every point in the plasma which becomes computationally prohibitive for large structures typical of most aerospace applications. However, if a plasma is strongly collisional so that the time scale of the inter-species collisions is shorter than the other characteristic times in the system, the plasma can be modeled as a mixture of ionized and neutral gases in thermo-chemical nonequilibrium, exerting electromagnetic forces[2] on one another.

Even with this fluid-like behavior of a plasma, it is computationally difficult and numerically complex to simulate the dynamics of a plasma. Modeling each of the numerous species results in a large system of equations that are numerically stiff because of the strong source terms from thermo-chemical nonequlibrium chemistry and electromagnetic forces. Therefore, traditionally, a number of simplifications and assumptions have been made about the dynamics of plasma that severely reduce the total number of equations and their complexity. In this work, however, we have attempted to take a different route and solve the full system of governing equations governing the behavior of every species in the plasma including the physics of thermo-chemical nonequilibrium.

Historically, the set of governing equations has been formulated by Lee[3] and consists of a set of Navier-Stokes equations describing the fluid behavior coupled with a set of Maxwell's equations governing the electromagnetic behavior. Since there are multiple species in a plasma, Lee's formulation consists of an equation for conservation of mass of every species. However, to reduce the size of the problem, the equations for conservation of momentum and energy are averaged over the various species. There is a separate equation for the conservation of energy of the electrons because electrons are much lighter than the ions and neutrals and exhibit very different dynamics from them. Thus, the full set of equations consists of a continuity equation for each species, a mass-averaged equation for conservation of momentum in every direction and one equation for the conservation of total energy of the heavy species and one for the electrons. Thus the temperature of all the species except the electrons, is assumed to be the same. In our work, we solve a full set of Navier-Stokes equations for each species and allow each species to vary in temperature as governed by the thermo-chemical nonequlibrium processes.

Since, in the described approach, there is only one set of momentum equations in the mass averaged formulation, the individual velocity of the various species is calculated as a sum of this mass averaged velocity and a diffusion velocity of that species. Additional equations are required to model this diffusion velocity of the species and close the system of equations. However, our formulation does not suffer from this closure problem because we solve a set of equations for conservation of momentum for every species.

In addition, Lee's formulation assumes that the ionized gases are charge neutral, meaning that the number of negatively charged particles equals the number of positive charged particles everywhere in the domain. This assumption holds well for plasma in subsonic flows however, MacCormack et al.[4] have shown that separation of charge can occur near shock waves in supersonic flows. Local separation of charge exerts strong electrostatic forces resulting in stiff governing equations. We drop the assumption of charge neutrality by employing the technique developed by MacCormack et al.[4] for calculating the electric field and reducing the stiffness in the governing equations.

In this paper, we present a new formulation for modeling high-temperature plasmas which solves a full set of Navier-Stokes equations for each species, augmented with source terms to include the thermo-chemical nonequilibrium and electrodynamics effects. There is an equation of conservation of mass, a set for conservation of momentum and one for conservation of energy for each species. The solution of the coupled set of Navier-Stokes equations for all the species is followed by the solution of Gauss's law from Maxwell's equations for the electric field. The complete set of Navier-Stokes equations for all the species is solved simultaneously at every time step. The solution procedure is unsteady and fully implicit in time. Finally, a Galerkin finite element formulation is used to solve Gauss's law once after every time step of the fluid equations. Although Argon gas is used in the present simulation, the procedure can be extended to any gas of interest with applications including entry through atmospheres on different planets. The development of these procedures has three goals:

1. Accurate representation of the governing equations,

2. High numerical efficiency in multidimensional flows,

3. Extension to solve real-world engineering applications, including (a) active flow control by plasma actuators, (b) reduced heat transfer to hypersonic vehicles and (c) assessment of possible blinding of electronic sensors of satellites upon micrometeroid impact.

The article is divided as follows: Section (2) describes the set of governing equations including the Navier-Stokes equations, Maxwell's equations and thermo-chemical nonequlibrium relations. Section (3) describes the numerical implementation of the governing equations. Section (4) presents two simulation test cases and comparisons with published data. Then a general conclusion of the work is presented.

2. Formulation of Equations Governing Reacting Flows at Hypersonic Speeds

The set of equations governing chemically reactive hypersonic flows includes the reacting Navier-Stokes equations governing the fluid properties and Maxwell's equation governing the electromagnetic behavior of the charged species in the flow.[2] In this section, we provide a brief description of the two sets of equations followed by the expressions for the chemical reactions for nonequilibrium flow. At the end of this section, we present the combined set of equations that are solved numerically.

A. The Navier-Stokes Equations

The Navier-Stokes equations defined in a closed domain, Ω, for compressible viscous flow of plasmas within an electromagnetic field are given by:

$$\frac{\partial U}{\partial t} + \nabla \cdot \vec{F} = \vec{S},\ in\ \Omega \in \mathbb{R}^3,\ t > 0, \tag{1}$$

where U is the vector of conservative variables and $\vec{F}$ and $\vec{S}$ represent the fluxes and source terms given as

$$U = \left\{ \begin{array}{c} \rho \\ \rho\vec{v} \\ \rho E \end{array} \right\},\ \vec{F} = \left\{ \begin{array}{c} \rho\vec{v} \\ \rho\vec{v} \otimes \vec{v} + \bar{\bar{I}}p - \bar{\bar{\tau}}) \\ \rho H\vec{v} - \bar{\bar{\tau}} \cdot \vec{v} - k\vec{\nabla}T \end{array} \right\},\ S = \left\{ \begin{array}{c} 0 \\ \vec{J} \times \vec{B} \\ (\vec{J} \times \vec{B}) \cdot \vec{v} + \dfrac{1}{\sigma_e}\vec{J} \cdot \vec{J} \end{array} \right\}. \tag{2}$$

The current density, $\vec{J}$, is determined from Ohm's law, $\vec{J} = \sigma_e(\vec{E} + \vec{v} \times \vec{B})$. $\vec{E}$ and $\vec{B}$ are the electric and magnetic field vectors determined from Maxwell's equations given in Eq. (3). The electrical conductivity σ_e depends upon the number and mobility of the charged particles present in the medium.

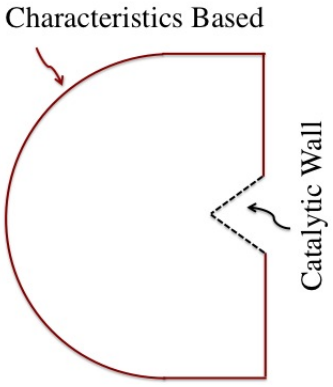

Figure 1. Schematic showing a set of boundary conditions for the fluid equations

The boundary conditions for the Navier-Stokes are given in Fig. (1). Due to the hyperbolic nature of the Navier-Stokes equations, the boundary conditions on the outer boundaries are based on the direction

of the characteristics of the governing equations. No-slip, catalytic boundary[2,5] conditions are used on the solid wall. A detailed description of catalytic boundary conditions is given in Section (4).

B. Maxwell's Equations

Maxwell's equations are a set of partial differential equations which together with the Lorentz's force law, form the foundation of classical electrodynamics. The usual form of Maxwell's equations is composed of Faraday's equation, governing the induction of the magnetic field, and Ampere's equation governing the induction of the electric field. In addition, two constraints defined by Gauss's law and Gauss's law for magnetism complete the set of Maxwell's equations. The complete set defined on a closed domain is given by:

$$\text{Faraday's law:} \quad \frac{d\vec{B}}{dt} = -\nabla \times \vec{E}, \qquad in\ \Omega \in \mathbb{R}^3,\ t > 0, \tag{3a}$$

$$\text{Ampere's law:} \quad \frac{\partial \vec{E}}{\partial t} = \frac{1}{\varepsilon_0}\left(\frac{\nabla \times \vec{B}}{\mu_0} - \vec{j}\right), \ in\ \Omega \in \mathbb{R}^3,\ t > 0, \tag{3b}$$

$$\text{Gauss's law:} \quad \nabla \cdot \vec{E} = \frac{\rho^c}{\varepsilon_0}, \qquad in\ \Omega \in \mathbb{R}^3,\ t > 0, \tag{3c}$$

$$\text{Gauss's law for magnetism:} \quad \nabla \cdot \vec{B} = 0, \qquad in\ \Omega \in \mathbb{R}^3,\ t > 0, \tag{3d}$$

where μ_e is the magnetic permeability of free space and is equal to $4\pi\times10^{-7}$ kg.m.C^{-2}. ϵ_o is the permittivity of free space and is equal to 8.854×10^{-12} C^2.s^2.kg^{-1}.m^{-3}. The current density $\vec{j}$ represents the moving charge within the flow, $\rho^c\vec{v}$, and that is driven by the electrical field via Ohm's law, $\vec{J} = \sigma_e(\vec{E} + \vec{v} \times \vec{B})$. Thus,

$$\vec{j} = \rho^c\vec{v} + \sigma_e(\vec{E} + \vec{v} \times \vec{B}), \tag{4}$$

where ρ^c is the charge density defined in Eq.(11)(d). In this paper, we expect the magnetic field created due to the movement of separated charge in the flow to be small and therefore neglect it. Thus, we only require the solution of Gauss's law to compute the electrodynamic effects of charge separation. The electric field is a conservative field and can be expressed as the gradient of a scalar electrostatic potential ϕ. Using this, Gauss's law can be expressed in terms of ϕ as,

$$\nabla^2\phi = -\frac{\rho^c}{\epsilon_0}. \tag{5}$$

Because of the elliptic nature of the governing equation, Dirichlet and Neumann boundary conditions are used for this problem.

C. Equations for Chemical Nonequilibrium Flows

When Argon gas is heated to very high temperatures, electrons in some atoms of the gas gain the proper amount of energy to escape the electric potential barrier and become free to move, leaving the atom singly positively ionized. The gas is then said to be partially ionized, consisting of mostly neutral Argon atoms along with some free electrons and an equal number of positive ions. The process of ionization in Argon is given by,

$$Ar + M \rightleftharpoons Ar^+ + e^- + M, \tag{6}$$

where M acts as a catalyst, contributing collisional energy, to enable the ionization reaction to take place, and it can be any of the three species present namely, an Argon neutral atom or an ion or an electron. The rate of reaction is given by,

$$R = \sum_s \left[-k_{f_s} X_n X_s + k_{b_s} X_i X_{e^-} X_s\right], \tag{7}$$

where X_s is the molar concentration of species s, $X_s = \rho_s/M_s$ in mole.m^{-3} and M_s is the molecular weight of species s, the value of which for the different species is given in the Appendix in Table (5). The rate of forward reaction for species s is k_{f_s} and the rate of backward reaction, k_{b_s}, is related to the rate of forward reaction and the equilibrium constant K_{e_s} by,

$$
\begin{aligned}
k_{b_s} &= k_{f_s}/K_{e_s} \text{ in m}^6.\text{s}^{-1}, && (8)\\
k_{f_s} &= C_s T_s^{\eta_s}\left(\frac{\theta_s}{T_s}+2\right) exp(-\theta_s/T_s) \text{ in m}^3.\text{s}^{-1}, && (9)\\
K_{e_s} &= C_{K_s} T_s^{\zeta_s} exp(-\phi_s/T_s) \text{ in m}^{-3}, && (10)
\end{aligned}
$$

where the values of the various constants in the above reaction rates are given in the Appendix in Table (4). The reaction rates for the ionization of Argon are taken from Hoffert and Lien[6] and Itikawa.[7]

D. The Full Set of Governing Equations and Boundary Conditions

Having defined the Navier-Stokes equations which describe the fluid dynamics of the plasma, Maxwell's equations which describe the electromagnetism in the plasma, and the rates of chemical reactions in plasma in Argon gas, we now combine the three sets of governing equations to come up with a set of equations that are numerically solved to simulate plasma in high speed flows of Argon gas. The final set of equations with the appropriate boundary conditions is given by,

$$
\begin{aligned}
&\frac{\partial \rho_s}{\partial t} + \frac{\partial \rho_s u_{s_j}}{\partial x_j} = w_s, && (11a)\\
&\frac{\partial \rho_s u_{s_k}}{\partial t} + \frac{\partial \rho_s u_{s_k} u_{s_j}}{\partial x_j} + \frac{\partial p_s}{\partial x_k} = -\frac{\partial \tau_{s_{j,k}}}{\partial x_j} + E_{mf_{s_k}} + Q_{u,s_k}, && (11b)\\
&\frac{\partial e_s}{\partial t} + \frac{\partial (e_s + p_s) u_{s_j}}{\partial x_j} = -\frac{\partial \tau_{s_{j,k}} u_{s_k}}{\partial x_j} - \frac{\partial q_{s_j}}{\partial x_j} + (E_{mf_{s_k}} + \quad Q_{u,s_k}) u_{s_k} + Q_{T_s}, && (11c)\\
&\nabla^2 \phi = -\frac{\rho^c}{\epsilon_0} = -\frac{e_c}{\epsilon_0}\left(\frac{\rho_i}{m_i} - \frac{\rho_{e^-}}{m_{e^-}}\right) = -\chi, && (11d)
\end{aligned}
$$

where the subscript s denotes the species, $s = \text{Ar}$, Ar^+ and e^-. The term w_s represents the rate of production of species s through ionization, dissociation, recombination etc. The term $E_{mf_{s_k}}$ represents the component of the electromagnetic force acting on gas s along k, which is non-zero only for the gases of charged species. The term Q_{u,s_k} represents the component of momentum transferred to gas s along k during collisions with other gases, and Q_{T_s} represents the energy transferred in the form of heat to gas s when it collides with other gases. The expressions for each of these source terms in the governing equations are given in the following subsections.

1. *The mass production terms*

$$
\begin{aligned}
w_n &= M_n R, && (12a)\\
w_i &= -M_i R, && (12b)\\
w_{e^-} &= -M_{e^-} R, && (12c)
\end{aligned}
$$

where M_s is given in the Appendix in Table (5) and the rate of reaction R is given in Eq. (7). The sum of the rates of formation of all species must be zero to conserve total mass, therefore $w_n + w_i + w_{e^-} = 0$.

2. Electromagnetic force

$$E_{mf_{s_k}} = \rho_s N_A \frac{Z_s}{M_s} e_c \Big(E_k + (\vec{v} \times \vec{B})_k \Big) = Z_s \frac{\rho_s}{m_s} e_c \Big(E_k + (\vec{v} \times \vec{B})_k \Big), \tag{13}$$

where N_A is Avogadro's number, the charge number, Z_s, is the number of electron charge on species s and is given in the Appendix in Table (5) for the various species. e_c is the unit charge on an electron, $m_s = M_s/N_A$ is the mass of one particle of species s given in the Appendix in Table (5), and $n_s = \rho_s/m_s$ is the number density of species s.

3. The Momentum transfer terms

$$Q_{u,n_k} = \rho_n \nu_{n,i}(u_{i_k} - u_{n_k}) + \rho_n \nu_{n,e}(u_{e_k} - u_{n_k}), \tag{14a}$$
$$Q_{u,i_k} = \rho_i \nu_{i,n}(u_{n_k} - u_{i_k}) + \rho_i \nu_{i,e}(u_{e_k} - u_{i_k}), \tag{14b}$$
$$Q_{u,e_k} = \rho_e \nu_{e,n}(u_{n_k} - u_{e_k}) + \rho_n \nu_{e,i}(u_{i_k} - u_{e_k}), \tag{14c}$$

where the subscript n is for neutrals, i is for ions and e is for electrons. The frequency of collision, $\nu_{r,s}$ is equal to $\frac{\rho_s \sigma_{r,s} \bar{c}_{r,s}}{(m_r + m_s)}$. The effective cross sectional area of collision, $\sigma_{r,s}$ is given by $\pi r_{r_s}^2$ where $r_{r,s}$ is the cross sectional radius. It is equal to $(d_r + d_s)/2$ if either of the colliding particles is a neutral particle, otherwise $r_{i,e} = r_{e,i} = \frac{e_c^2}{32\epsilon_0 k_B T_e}$. The relative collision speed, $\bar{c}_{r,s}$ is given as $\sqrt{\bar{c}_r^2 + \bar{c}_s^2}$ where $\bar{c}_s$ is the speed of species s given as $\sqrt{\frac{8k_b T_s}{\pi m_s}}$ where k_b is Boltzmann's constant. The sum of momentum transfer by collision to all species should be zero for momentum to remain conserved, thus, $Q_{u,n_k} + Q_{u,i_k} + Q_{u,e_k} = 0$.

4. The Heat transfer terms

$$Q_{T_n} = 2\rho_i C_{v_i} \nu_{n-i} \frac{m_i}{m_n}(T_i - T_n) + 2\rho_e C_{v_e} \nu_{n-e} \frac{m_e}{m_n}(T_e - T_n), \tag{15a}$$
$$Q_{T_i} = 2\rho_i C_{v_i} \nu_{n-i} \frac{m_i}{m_n}(T_n - T_i) + 2\rho_e C_{v_e} \nu_{i-e} \frac{m_e}{m_i}(T_e - T_i), \tag{15b}$$
$$Q_{T_{e^-}} = 2\rho_e C_{v_e} \nu_{i-e} \frac{m_e}{m_i}(T_i - T_e) + 2\rho_e C_{v_e} \nu_{n-e} \frac{m_e}{m_n}(T_n - T_e), \tag{15c}$$

where ν_{r-s} is the relaxation parameter, obtained experimentally and taken from Hoffert and Lien,[6] with

$$\nu_{n-e} = \nu_{e-n} = \frac{\rho_n}{m_n}\sqrt{\frac{8k_B T_e}{\pi m_e}}(-0.39 - 0.551 \times 10^{-4} T_e + 0.595 \times 10^{-8} T_e^2) \times 10^{-20}, \; T_e < 10,000^\circ K, \tag{16a}$$
$$\nu_{n-e} = \nu_{e-n} = \frac{\rho_n}{m_n}\sqrt{\frac{8k_B T_e}{\pi m_e}}(-0.35 + 0775 \times 10^{-4} T_e) \times 10^{-20}, \qquad T_e > 10,000^\circ K, \tag{16b}$$
$$\nu_{i-e} = \nu_{e-i} = \frac{\rho_{e^-}}{m_{e^-}}\sqrt{\frac{8k_B T_e}{\pi m_e}} max(1.95 \times 10^{-10} T_e^{-2} Log(1.53 \times 10^{14} T_e^{-3} \frac{m_e}{\rho_e}), 0). \tag{16c}$$

The value of ν_{n-i} was estimated to be equal to ν_{e-i}. The sum of heat transfer by collision to all species should be zero for energy to remain conserved, thus, $Q_{T_n} + Q_{T_i} + Q_{T_{e^-}} = 0$.

3. Numerical Implementation

The equations have been coded in a tool suite named SU^2 (Stanford University Unstructured), an open-source collection of software tools written in C++ for performing analysis of Partial Differential Equations

(PDE) and solving PDE constrained optimization problems. SU^2 solves a discretized version of the integral form of the Navier-Stokes equations using a finite volume method with a standard edge-based discretization on a dual control volume. The semi-discretized integral[8] form of the Navier-Stokes equation is given by,

$$\int_{\Omega_i} \frac{\partial U}{\partial t} d\Omega + \sum_{\partial\Omega_i} (\vec{\hat{F}}_c \cdot \vec{n}) \Delta S + \sum_{\partial\Omega_i} (\vec{\hat{F}}_v \cdot \vec{n}) \Delta S = Q\Omega_i, \tag{17}$$

where U is the vector of state variables. $\vec{\hat{F}}_c$ is the numerical approximation of convective fluxes, $\vec{\hat{F}}_v$ is the numerical approximation of viscous fluxes, and Q is the vector of the source terms. $\vec{n}$ is the inward unit normal, ΔS is the area of the face and $\delta\Omega$ is the bounding surface of the control volume. The calculations are performed using a three-dimensional formulation. There are three species present in Argon plasmas at high temperatures, namely, neutral Ar atoms, Ar^+ ions, and free electrons. Each species has been modeled as a different gas in this formulation. There is a set of five conservation equations for each species, and a coupled system with a total of 15 reacting Navier-Stokes equations is solved, followed by a converged solution of Gauss's law from Maxwell's equations at the end of each time step of the fluid equations. The flow equations for the three gases are integrated in time using a Backward Euler method (1^{st} order in time). Implicit time stepping is employed to advance the solution in time and to allow large physical time steps without running into numerical stability constraints of the time integration process. In addition, using implicit schemes helps alleviate numerical stiffness issues because these methods are known to be robust with superior convergence speed particularly for the case of strong source terms coming from thermo-chemical nonequilibrium chemistry relations.

The convective fluxes are spatially discretized using Roe's[9] first-order flux difference splitting scheme, that is well known for excellent resolution of boundary layers and a crisp representation of shock waves. The viscous fluxes are discretized using a central difference procedure. In order to evaluate the viscous fluxes, flow quantities and their first derivatives have to be known at the faces of the control volumes and, due to the elliptic nature of the viscous fluxes, the values of the flow variables including the velocity components, the dynamic viscosity μ, and the heat conduction coefficient k are simply averaged at a face. The gradients of the flow variables are calculated using a Green-Gauss method over the cell nodes and then averaged to obtain the gradients at the cell faces.

The resulting linear system of equations is solved using a symmetric Gauss-Seidel relaxation technique. For unsteady plasmas, the fluid equations are converged at every time step while convergence acceleration techniques like local time stepping and multigrid methods are used for steady-state solutions.

For solving the electrostatic potential equation, a finite element-based formulation with piecewise constant integration of source terms is used. The electrostatic forces produced by separation of charge in the flow are very strong and restrict the time step for the flow equations to exceedingly small values. This, in turn, requires significant computational power and is a reason why local charge separation is not generally included in most simulations. MacCormack[4] et al. have presented a novel technique that mitigates this problem through the development of an additional equation for the electric field relaxation, based on Newton's laws of motion. The technique allows a much greater time step for the flow equations and the use of implicit methods to advance the flow solution in time. It involves the derivation of an additional equation that enables the solution of Gauss's law to proceed at the same rate as allowed by the flow equations. The method is presented here in short but the reader is referred to the original paper[4] for more details. The parameter χ appearing in Gauss's law in Eq.(11) is evaluated after the equations for the electrons and ions have been solved as:

$$\chi^n = \frac{e_c}{\epsilon_0} \left(\frac{\rho^n_{e^-}}{m_{e^-}} - \frac{\rho^n_i}{m_i} \right). \tag{18}$$

The value of χ^n above is valid at the beginning of a time step of size Δt , used to solve the flow equations, but probably not over the complete time step interval when significant change may occur. The parameter χ^n can change rapidly under the exceedingly strong electromagnetic forces acting on the electrons and ions to reduce charge separation. For this reason, MacCormack et al.[4] developed a new equation for the time

evolution for χ^n over the time interval Δt from the species continuity and momentum equations

$$\frac{\partial \chi}{\partial t} = \frac{e_c}{\epsilon_0}\left(\frac{1}{m_e}\frac{\partial \rho_e}{\partial t} - \frac{1}{m_i}\frac{\partial \rho_i}{\partial t}\right) = -\frac{e_c}{\epsilon_0}\left(\frac{1}{m_e}\frac{\partial \rho_e u_{e_j}}{\partial x_j} - \frac{1}{m_i}\frac{\partial \rho_i u_{i_j}}{\partial x_j}\right). \tag{19}$$

This equation is then discretized over the time step Δt, followed by the application of Newton's law to calculate the velocity at the next time step under the application of electric field. The final expression for χ^{n+1} is

$$\chi^{n+1} = \frac{1}{1+\alpha}\left\{\chi^n - \Delta t \frac{e_c}{\epsilon_0}\left(\frac{1}{m_e}\frac{D\cdot \rho_e^n u_{e_j}^n}{\Delta x_j} - \frac{1}{m_i}\frac{D\cdot \rho_i^n u_{i_j}^n}{\Delta x_j}\right)\right\}, \tag{20}$$

where $D\cdot/\Delta x_j$ is the difference operator, subscript e is for electrons, subscript i is for ions, and $\alpha = \Delta t^2 \frac{e_c^2}{\epsilon_0}\left(\frac{\rho_e^n}{m_e^2} + \frac{\rho_i^n}{m_i^2}\right)$. This implicit treatment of the source term, χ, on the right side of the electric potential equation, with very large values of α, is sufficient to control the numerical stability of the difference equation and permits the electric equations to be advanced with the same large time steps as the flow governing equations.

4. Simulation Test Cases

Two test cases for plasma in high speed Argon gas were simulated and the results were compared with literature and experiments which showed excellent matches. In the first test case, we solved for unsteady dynamics of plasma near a normal shock wave at Mach 15. In the second case, heat transfer from a Mach 4.6 plasma stream to a three dimensional body was numerically measured and the result of heat flux were compared with experiments done at NASA Langley which showed an excellent match.

A. Test Case 1: Unsteady Plasma Dynamics near a Normal Shock at Mach 15

A stream of Argon gas moving at Mach 15, passing through a normal shock wave and resulting in the formation of a plasma in the vicinity of the shock was numerically simulated and verified with results by MacCormack et al.[4] The domain for this computation was 4 mm long in the x direction and 0.8 mm long in the y direction, and we used 82 equally-spaced points in the x direction and 5 in the y direction. The domain in x direction varied from [-0.002, 0.002] m.

1. Initial Condition

Since this was an unsteady simulation with multiple chemically reacting species, it was important to choose a physically-feasible set of initial conditions which satisfied conservation of charge. For this reason, we provide a detailed description of the initial conditions used. The solutions obtained by our solver were tested to be robust to most choices of these physically-feasible initial conditions.

For the purpose of explaining the initial conditions, we have divided the domain into two parts: the part upstream of the shock wave has been referred to as the left half of the domain and the part downstream of the shock has been referred to as the right half of the domain. The left half of the domain spans from x = [-0.002 to 0.0] m and the right half from (0.00 to 0.002] m. Since there are multiple species present in the flow, we define a set of initial conditions for each species.

Left-Half Domain: The temperature of each species is set equal to 300 K. The density of Argon atoms is 0.21331 kg/m^3. We start with a small degree of ionization of 0.1% which makes the density of ions equal to 0.21331×10^{-3} kg/m^3 and that of electrons equal to 2.9313×10^{-9} kg/m^3. The velocity of all three species is the same, 4800 m/s in the x direction. This velocity corresponds to Mach 15 for the Argon atoms and ions, and Mach 0.05 for the electrons at 300 K. This disparity in Mach numbers is due to the fact that electrons have a very small mass and thus a high gas constant that leads to a very high speed of sound for electrons.

On the other hand, the masses of the atom and the ion are nearly equal and therefore the speed of sound in the two gases is the same.

Table 1. Flow initial conditions in left-half domain, x = [-0.002, 0] m

Quantity	Argon	Ion	Electron
Temperature (K)	300	300	300
Density (kg/m^3)	0.2133	0.2133 $\times 10^{-3}$	2.9313 $\times 10^{-9}$
Velocity (m/s)	(4800, 0, 0)	(4800, 0, 0)	(4800, 0, 0)
Mach	15	15	0.05

Table 2. Flow initial conditions in right-half domain, x = (0, 0.002] m

Quantity	Argon	Ion	Electron
Temperature (K)	21000	21000	300
Density (kg/m^3)	0.8418	0.8418 $\times 10^{-3}$	1.156 $\times 10^{-8}$
Velocity (m/s)	(1200, 0, 0)	(1200, 0, 0)	(1200, 0, 0)
Mach	0.44	0.44	0.0125

Right-Half Domain: The flow properties of the gases that were supersonic on the left-half domain, namely the Argon atoms and ions, were expected to be different from the electrons which moved subsonically in the left-half domain and, therefore, we started with a different set of initial conditions for the gases on the right-half domain. For the ion and neutral atom gases, we started with flow conditions governed by the normal shock jump relations. The density of the neutral gas was set to 0.842 kg.m^{-3} and the density of the ion gas was 0.842×10^{-3} kg.m^{-3}, the temperature of these gases also increased as they passed through the shock wave and was calculated by the normal jump relations to be equal to 21,000 K . The speed of these two gases decreased to maintain the incoming mass flow rate and was thus set to 1200 m.s^{-1}. On the other hand, due to the large speed of sound for electrons, they were subsonic in the left-half domain and did not experience a shock wave. Their temperature remained at 300 K on the right-half domain. We would think that their density should have remained the same too, but because of an increase in the ion density in the right-half plane, the electron density also jumped up to guarantee charge conservation: there has to be an electron for every ion in the flow. The density of electrons was thus set equal to 1.156×10^{-8} kg.m^{-3}. The speed of electrons decreased in proportion to the increase in density to maintain mass conservation and equaled 1200 m.s^{-1}.

Because we start the flow with the condition of neutrality of charge everywhere in the domain, the electrostatic potential was constant everywhere in the domain and was set equal to zero.

2. Boundary Conditions

This test problem is a one-dimensional problem solved in a two-dimensional formulation. For this reason, the upper and lower boundaries have symmetric boundary conditions imposed on them. Characteristics-based inlet boundary conditions are imposed on the left boundary. Characteristics-based outlet boundary conditions are not used on the right boundary because the pressure at the outlet is unknown for this problem. Before the flow comes to thermal equilibrium, there is a significant increase in the density and the temperature of electrons resulting in an increase in its pressure by orders of magnitude. The pressure at the outlet is thus not a known quantity and therefore Neumann boundary conditions were used on the right boundary.

The electrostatic potential equation solves for a scalar-valued function, ϕ, we can fix its value at the left boundary and every other value would be relative to this. Neumann boundary conditions are used on the right boundary.

3. *Results and Discussion*

As the flow evolves with time, we observe very interesting physics involving fluid dynamics of a mixture of gases at vastly different Mach numbers, highly coupled with the chemistry of gases at high temperature, and along with electrodynamics of charged particles. We start a discussion of the results with the electrons because they were subsonic and showed some particularly interesting features.

Electrons masses are more than 4 orders of magnitude smaller mass than the ions or the neutral atoms in this flow. Therefore their gas constant is much larger than that of the ions or the atoms. A large gas constant makes the speed of sound in electrons very high, which in turn makes the Mach number of the electrons very small compared to that of ions/atoms for the same bulk velocity. This situation divides the flow into a group of gases moving at hypersonic speeds of Mach 15 and the electrons which were subsonic at Mach 0.05. Because the electrons were subsonic, we started with a uniform temperature of 300 K for the electrons everywhere in the domain as shown in Fig. (2)(a). The rest of the gases experienced a shock wave and were at a much higher temperature behind the shock wave. The electrons collided and exchanged energy with these gases at high temperatures and gained energy as shown in Fig. (2)(b). The electron temperature quickly increased and ultimately came into a thermal equilibrium with the rest of the gas as shown in Fig. (2)(c) and (d). Because the temperature of the various species was very high behind the shock wave, more of the Argon atoms ionized into ions and electrons. Thus, the density of electrons and ions increased on the right-half domain as shown in Fig. (3)(a). The process of ionization takes up a significant amount of energy to free the electron from an atom. Therefore, the temperature of the flow on the right half plane decreased as shown in Figures (2)(d-f).

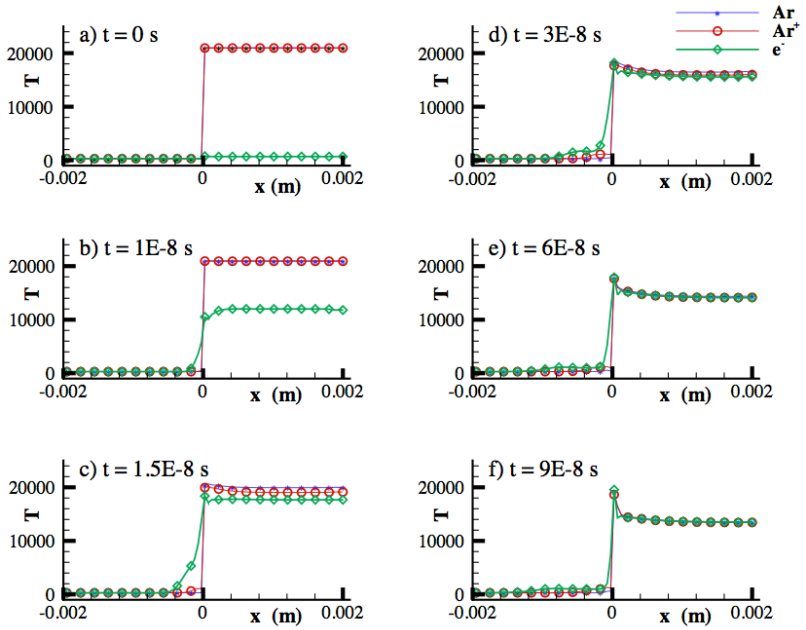

Figure 2. The asterisks indicate the neutral gas, the circles are for the ionized gas and the diamonds indicate the electrons. The figure shows evolution of temperature of the flow with time until all gases come into thermal equilibrium. (a) shows a rise in temperature for ions and atoms moving at Mach 15 as they pass through the shock wave. The electrons being subsonic at M = 0.05 maintain their temperature at 300 K. (b) The electron temperature rises by colliding with gases at higher temperature. (c) The temperature of the electrons has reached an equilibrium with the rest of the gases. (d) Temperature of the flow decreases to compensate for the expenditure of energy in ionization. (e) Further decrease in temperature due to ionization. The small peak at the location of the shock wave is due to lack of viscosity. (f) As the flow temperature decreases, the rate of ionization slows down, thus decreasing the rate of temperature fall and the flow comes to an equilibrium temperature.

Figure (3) shows how the density of electrons evolved with time, we see that the density has increased both upstream and downstream of the shock. The increase downstream of the shock is due to the process of ionization resulting in more electrons behind the shock. However, the rise in the density of electrons upstream of the shock is owing to their subsonic Mach number. Given the increase in density and pressure downstream of the shock, the partial pressure of the electrons also increases and, because the electrons were subsonic, information was able to propagate upstream and cause an increase in the density of the electrons upstream of the shock. However, ions were supersonic upstream of the shock and information could not travel upstream in ions and, therefore, there wasn't an increase in the density of the ions just upstream of the shock wave. This local bunching of negative charge upstream of the shock and a small dip at the shock wave caused charge separation near the shock wave. Separation of charge exerts very powerful forces on the charged species changing the flow properties in the vicinity of the shock: this is why it is important to model the phenomenon of charge separation in a simulation of plasma. The electrons were accelerated to values higher than the mean flow upstream of the shock as shown in Fig. (4)(c). Normalized values of the electrostatic potential and electric field are shown in figure (4) (a).

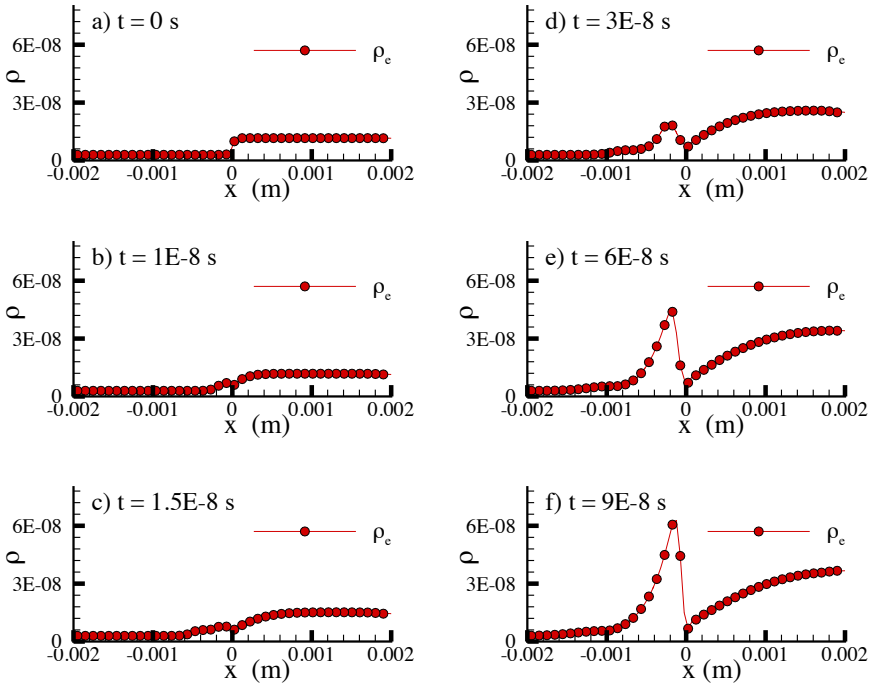

Figure 3. The figure shows the evolution of density of electrons with time. (a) shows that the density of electrons is high on the right-half domain even though they are subsonic. Electrons have a much higher speed of sound and the speed that corresponds to Mach 15 for the ions, corresponds to Mach 0.05 for the electrons. The ion density rises downstream of the shock. For charge conservation, we must have an electron for every positively charged ion, thus the density of the subsonic electrons rises too. (b) The density of electrons continues to rise behind the shock wave due to ionization on the right-half domain. (c) The electron density is still rising with time which means that the temperature of the neutral gas is still high enough to support ionization. (d) Electrons are subsonic, the effect of density and pressure rise is being felt upstream. This results in a local collection of negative charge just upstream of the shock wave. (f) There is a significantly high increase in density of electrons upstream of the shock wave, because of this there is also a little dip in electron density at the shock location. (g) There is a very high increase in density of electrons upstream of the shock wave.

The test problem of the normal shock wave in Argon was used to verify the numerical program with results published by MacCormack[4] et al. Figure (4) shows the comparison of obtained results and published results. There is a very good match in the flow as well as the electrodynamic quantities between the published results and the current results. Note that the published results include viscosity and are second-order accurate in space and time.

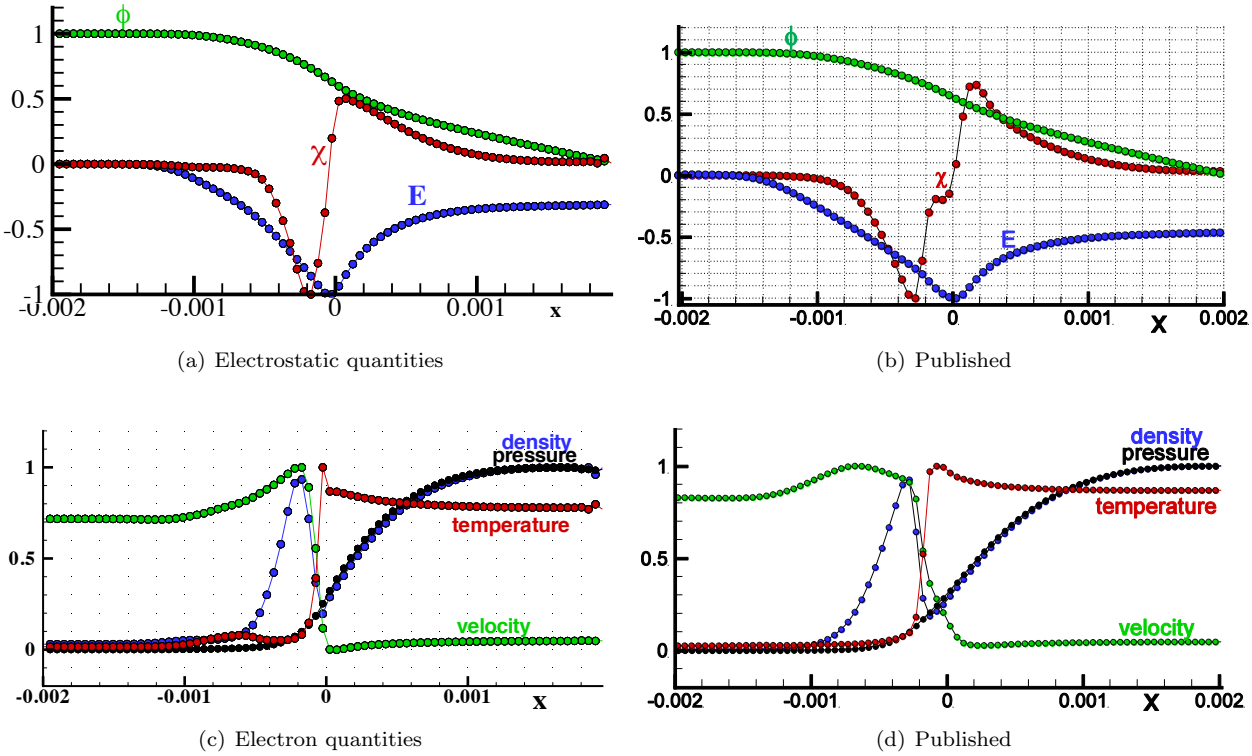

(a) Electrostatic quantities

(b) Published

(c) Electron quantities

(d) Published

Figure 4. Comparison with published work by MacCormack et al.[4] The differences near the shock wave are because published results include viscosity while current results don't. In addition, the current results are 1st order accurate in space while published results are second order.

B. Test Case 2: Heat Transfer to a shell in a 3-D Plasma Flow

In this test case we simulate a flow of partially ionized Argon gas and compute the heat transfer to a three-dimensional surface from this plasma stream. The results for the computed heat flux at the wall are then compared with experiments performed at NASA Langley by R. J. Nowak et al.[10] In the experiment, measurements of heat transfer to a hemispherical shell in a low density plasma in Argon were carried out. Argon gas was passed over a d.c. arc heater which ionized it to 1% and this stream of ionized Argon was expanded to Mach 4.6 through a nozzle at the end of which measurements of flow parameters such as the electron temperature, density and others were made. A bullet shaped shell with a hemispherical nose was tested in this plasma stream and the heat transferred to the shell from the plasma stream was measured at various locations along the nose. We numerically simulated this plasma stream and computed the heat flux to the model and validated our results with the experiments.

1. Numerical Procedure

The governing equations of the flow are given in Section (2). The equations were solved iteratively in time to a steady-state value until the maximum residual in the flow variables of each species in the domain

decreased by 4 orders of magnitude. The drop in residual of the ions was 2.5 orders. Since the problem of interest was steady, local time stepping[11] was used to accelerate convergence: the discretized governing equations were integrated using the largest possible time step for each control volume. As a result, the convergence to the steady state was considerably accelerated, however the transient solution was no longer temporally accurate. To further accelerate convergence to steady state, the multigrid technique[12] based on the solution of the governing equations on a series of successively coarser grids was employed.

Even with these convergence acceleration techniques, the rate of convergence of the various species to a steady state was slow. This was because we were advancing all the species with the same time step chosen to be the smallest of the maximum allowed time steps of the three species. The maximum allowed time steps of the various species for a stable viscous calculation were different by a few orders of magnitude because of a large difference in the densities of the three species. To circumvent this problem, we advanced each species at its own maximum time step allowed for a stable calculation at a grid point and this accelerated the rate of convergence of the species by several orders of magnitude. In other words, each species was advanced at a different time step at every point in the grid. This was permitted because the problem of interest was steady.

Electric forces were not included in this problem because the large time steps of the fluid equations relaxed the local electric field to small values governed by Eq.(20). These small electric forces did not affect the flow solution much, but the solution of Gauss's law for calculating these forces considerably increased the computational time. Therefore, these forces were omitted from this three-dimensional calculations.

Sutherland's law was used to scale the viscosity of the various species with temperature. The viscosity of Argon ions at room temperature was assumed to be the same as that of Argon gas whereas the electrons were considered inviscid. Heat flux from all the fluids to the shell was added to obtain the total heat flux to the shell.

2. *Assumption of Continuum*

Since the density of the Argon gas was low in the experiment, it was necessary to ensure the existence of continuum everywhere in the domain and verify that the Navier-Stokes equations could be used to simulate the flow. Continuum can be assumed in flows where the mean free path of molecules is much smaller than a characteristic length in the domain. The mean free path is the average distance travelled by a particle between two collisions and is defined as

$$\lambda = \frac{1}{\sqrt{2} n \sigma}, \tag{21}$$

where λ is the mean free path, n is the number density given by $\frac{\rho}{m}$ and σ is the cross sectional area of collision given by πr^2. For our problem of interest, $n = \frac{1.664 \times 10^{-4}}{6.6 \times 10^{-26}} = 2.5 \times 10^{21}$ m^3, the cross sectional area $= \pi \times (4 \times 10^{-10})^2 = 5 \times 10^{-19}$ m ^{2} which makes the mean free path is equal 0.00056 m. The Knudsen number (K_n) defined as the ratio of the mean free path and a characteristic length of the domain, which is the radius of the shell here is equal to 0.03. Continuum can be assumed to exist if K_n is much smaller than 1.0 and given K_n is 0.03 for this flow, we proceed with a fluid-like approximation and use the Navier-Stokes equations to simulate the flow. Note that this value of K_n is a slightly conservative estimate as we calculated the mean free path based on the density of the flow upstream of the shock, but since the goal of the simulation is to measure the heat transfer rate, our interest lies mainly in the region downstream of the shock where the mean free path would be even smaller and K_n would be around 0.008.

3. *Computational Grid*

Since there are three species in the fluid, the simulations took a lot longer than a single species viscous simulation so the mesh had to be carefully designed to capture the important features of the flow field with as few points as possible. A hybrid, multi-block, pre-adapted, three-dimensional mesh was used for this simulation. Figure (5) shows the computational mesh. Since the main goal of the simulation was to measure the heat flux to the shell, it was essential to accurately resolve the boundary layer over the shell. It is generally advisable to employ 3D prismatic or hexahedral elements near solid walls for good resolution of

the boundary layer.[13,14] Therefore, the mesh consisted of structured elements with hexahedral cells close to the shell. The mesh was used to run a flow solution and obtain the probable location of the shock wave and the height of the boundary layer. This information was used to again refine the mesh around the probable location of the shock and around the solid wall to capture the shock and the boundary layer well. In order to simulate the jump in temperature of electrons from an inlet value of 3900 K to an equilibrium value of about 800 K in the interior of the domain, a few extra points were added near the inlet. Exploiting symmetry in the azimuth direction, only a 15 degree slice of the body with 7 equally spaced planes in the azimuth direction was simulated.

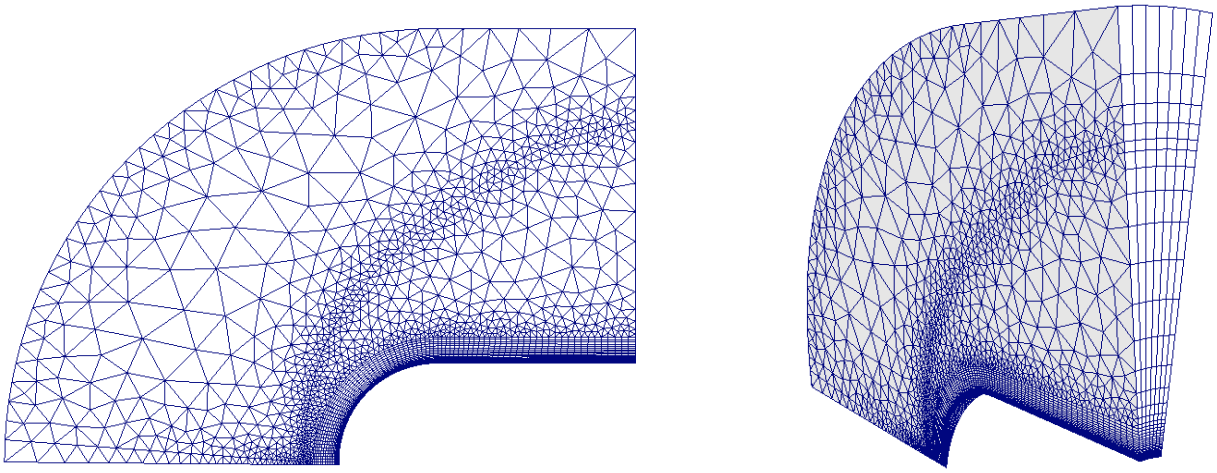

Figure 5. A hybrid mesh with 46,000 cells for a 3D simulation of a plasma stream over a hemisphere. This mesh is pre-adapted to capture the shock wave and the boundary layer well.

4. Initial Condition

The flow for the three species was started with values corresponding to the inlet conditions given in Table (4). These conditions were back calculated from the the density, mass flow rate and Mach number values from the experiment.

Table 3. Flow initial conditions

Quantity	Argon	Ion	Electron
Temperature (K)	810	810	3900
Density (kg/m^3)	1.664×10^{-4}	1.664×10^{-6}	2.29×10^{-11}
Velocity (m/s)	(2347, 0, 0)	(2347, 0, 0)	(2347, 0, 0)
Mach	4.6	4.6	0.025

5. Boundary Condition

Flow properties at the inlet and the outlet boundaries were chosen based on the direction of the characteristics of the governing equations. The sign of the eigenvalues of the governing equations determines the direction of the characteristics and this information is used to pick the characteristic variables from inside or outside of the domain at the boundaries. Catalytic boundary conditions were used on the wall of the shell. The wall can act as a catalyst promoting chemical reactions, namely the recombination of ionized species into atomic species, thus, moving toward equilibrium with the cooler wall. The wall temperature

was maintained at 300 K which for Argon in equilibrium would consist of only Argon neutral atoms. The environment at the wall promoted recombination reactions, for example,

$$Ar^{+} + e^{-} \rightarrow Ar. \tag{22}$$

The wall provided a complex surface chemistry beyond that of just a relative cool temperature. The recombination reactions released heat, which increased the heat transfer into the cooler wall. From a microscopic point of view, the average kinetic energy of species s is represented by $\frac{1}{2} m_s \bar{c_s}^2$, which according to the equi-partition of energy is equal to $\frac{3}{2} K_b T_s$. Solving for the molecular speed $\bar{c_s} = \sqrt{\frac{3K_b T_s}{m_s}}$. This speed is distributed about a solid angle of 4π steradians. The number flux of molecules of species s directed toward the wall can be shown to be

$$F_s = N_s \frac{1}{4} \sqrt{\frac{8K_b T_s}{\pi m_s}}, \tag{23}$$

where N_s is the number density, m_s is the mass and T_s is the temperature of species s. K_b is the Boltzmann constant. The wall was fully catalytic for the ions, i.e. all the ions coming towards the wall recombined with electrons to form Argon atoms. Thus, the rate of formation of the different species at the wall was calculated to be:

$$R_i = -\frac{\rho_i}{4} \sqrt{\frac{8K_b T_i}{\pi m_i}}, \tag{24a}$$

$$R_e = -\frac{m_e}{m_i} R_i, \tag{24b}$$

$$R_n = -(R_i + R_e), \tag{24c}$$

where R_s is the rate of recombination of species s. Heat released during recombination at the wall was transferred to the wall through an isothermal wall boundary condition. The wall was isothermal for ions and neutrals and adiabatic for the electrons. A no-slip boundary condition guaranteed zero velocity at the wall. Since the shell was at zero angle of attack with respect to the incoming free stream, symmetry boundary conditions were imposed in the azimuth direction. For a symmetry boundary, there is no flux across the boundary which is equivalent to the requirement that the velocity normal to the symmetry boundary is zero.

6. Results and Discussion

The rate of heat transfer from a flow to a solid body is given by,

$$Q = \kappa \, \partial_n T, \tag{25}$$

where, T is the temperature, and κ is the coefficient of thermal conductivity of the fluid defined as $\frac{C_p \mu}{P_r}$ where C_p is the specific heat capacity at constant pressure, μ is the viscosity and P_r denotes the Prandtl number. Since there are multiple species in this simulation, the contributions to heat transfer from every species in the plasma were summed to obtain the total amount of heat transferred to the shell. Figure (6) shows the numerically computed heat flux to the shell along the nose, compared with the experiments. The heat flux is highest near the nose of the hemisphere because the bow shock is strongest there, resulting in the maximum increase in temperature behind the shock. There is a very good match between the experiments and simulations.

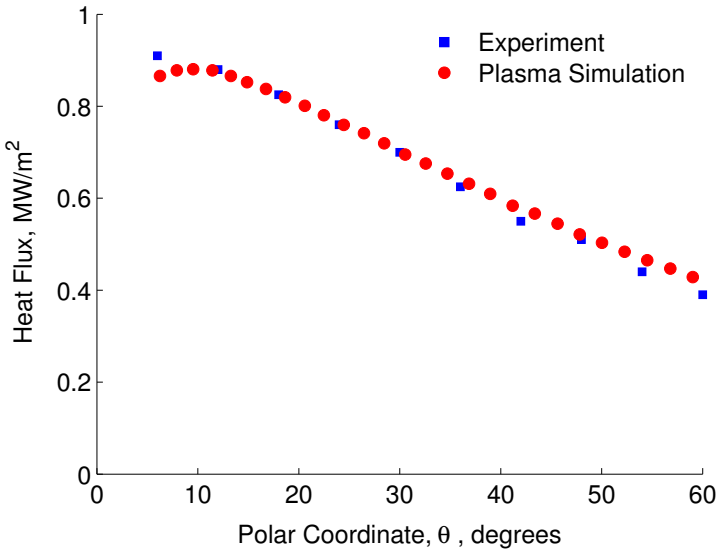

Figure 6. Comparison of numerical heat flux to the three dimensional shell from a supersonic stream of plasma in Argon with experiments done at NASA. The x axis is the polar coordinate along the nose of the shell and the y axis is the heat flux to the surface.

Now, let us look at the breakdown of the heat flux from the different species. Firstly, because the electrons were considered inviscid, their coefficient of thermal conductivity was zero and they did not transfer heat to the shell. Only the Argon neutrals and ions transferred heat to the shell. The heat transferred to the shell by the Argon neutral atoms and ions was similar because their temperature profiles were very similar. However, intuitively, one would expect that because the density of the ions was very small compared to that of the neutrals, the heat transferred by the ions would be small compared to the neutrals. Surprisingly, the heat transferred to the shell by the two species is comparable. This is because the expression for heat flux is independent of the density of the fluid, it is only a function of the gradient in temperature of the fluid and the wall and the coefficient of thermal conductivity. Given that the temperature of the ions and neutrals was similar, the heat transferred by the two species was comparable. This insight also reinforces that if one wants to measure the heat flux from a multi-species plasma to a solid wall, then it is very important to accurately model the dynamics of each of the species correctly.

The solution of this simulation includes many other interesting features. Because of the much smaller mass of electrons compared to the ions and neutrals, the speed of sound in the electrons was much higher than the speed of sound in the ions or neutrals. Therefore, for the same velocity, the Mach number of electrons was much smaller than that of the ions and neutrals. There was a difference of two orders of magnitude in the Mach numbers of the electrons and the other two species; the ions and neutrals were supersonic at Mach 4.6 while the electrons were low subsonic at Mach 0.03. This difference in Mach number resulted in different flow physics for the electrons and the other two species.

We first discuss the physics of the supersonic species, namely, the ions and the neutrals. We had started the flow of all the species with a uniform distribution of the flow variables, and as the simulation progressed, a bow shock appeared in front of the shell for these species, causing an increase in the density and temperature behind the shock wave. Figure (7) shows the distribution of the Mach number of the two supersonic species, the bow shock is strongest with the highest drop in Mach number near the axis where it is nearly normal. The Mach number near the wall is zero to ensure no-slip boundary conditions.

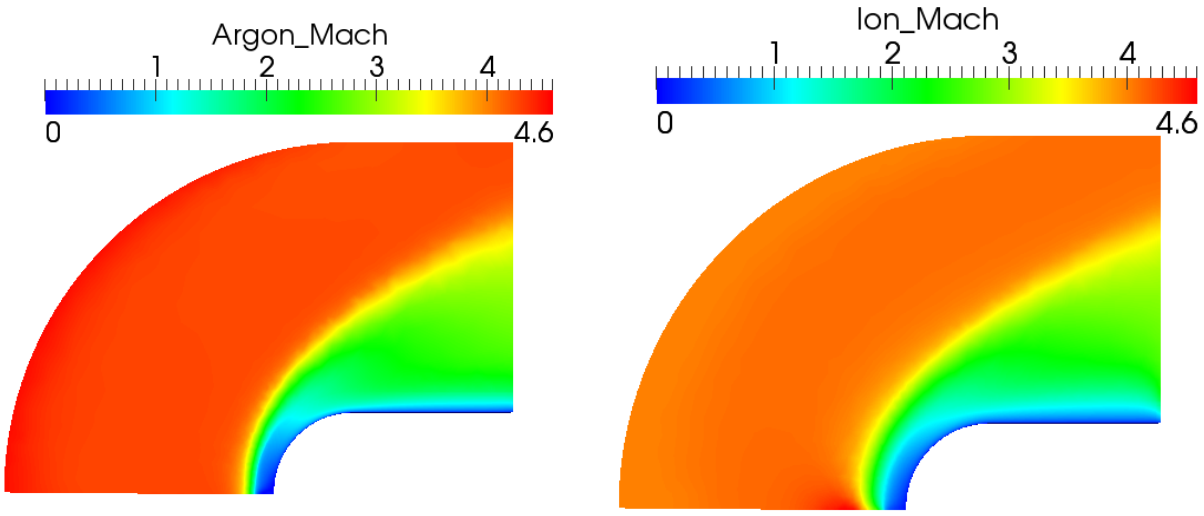

(a) Neutral Argon Mach number

(b) Argon Ion Mach number

Figure 7. Distribution of Mach number of the Argon neutral atoms and ions over the domain. These two species move supersonically and experience a bow shock.

Figure (8) shows the distribution of the temperature of the two heavy species. These two species were started with a temperature of 810 K everywhere in the domain, and as expected, they remained at 810 K upstream of the shock with an increase in temperature behind the shock. The solid body was maintained at 300 K throughout the experiment, and because it was relatively cooler than the surrounding fluid, heat was transferred from the two gases to the wall which resulted in a drop in temperature of the gases near the wall.

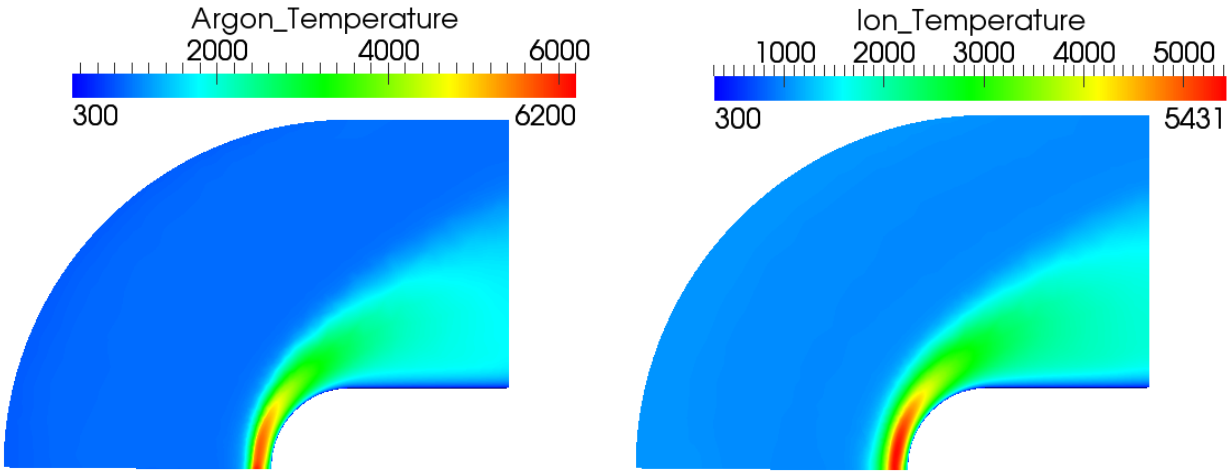

(a) Neutral Argon Temperature

(b) Argon Ion Temperature

Figure 8. Distribution of Temperature of the Argon neutral atoms and ions over the domain

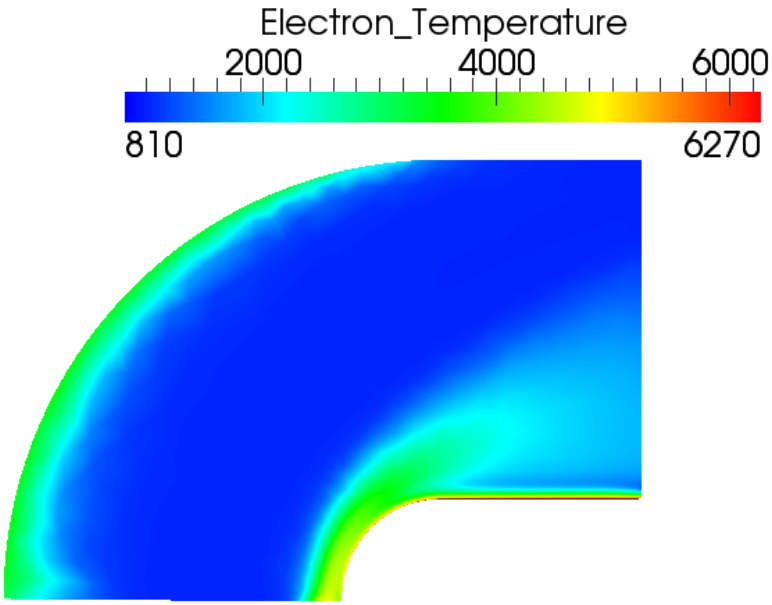

Figure 9. Distribution of the temperature of the electrons. The electrons were subsonic and did not see a bow shock, however, because the other two species were supersonic and experienced a shock wave, their temperature increased behind the shock. This difference in temperature of the species led to an increase in temperature of the electrons behind the shock wave till all the three species came into a thermal equilibrium. The inlet temperature was fixed at 3900 K by the d.c. arc heater.

The temperature of the subsonic species, namely the electrons, also showed interesting features. We had started with a uniform temperature of 3900 K everywhere for the electrons but the neutrals and ions, on the other hand, were started with a uniform temperature of 810 K, both corresponding to the far-field conditions in the experiment. Because of this difference in the temperature of the electrons and other species, an exchange of energy in between species took place by collision; electrons lost energy by colliding with the ions and neutrals and came to a thermal equilibrium with them. This lowered the temperature of the electrons to nearly 810 K, same as the ions and neutrals, in regions upstream of the shock for them. The temperature of the electrons dropped significantly till they reached thermal equilibrium with other gases. However, there wasn't a noticeable increase in the temperature of the ions and neutrals. This was because the density of the neutrals and the ions was much larger than that of the electrons, so the rise in temperature for the heat transferred to them from the electrons was very small. The electron temperature increased from 3900 to match the ion and neutral temperature behind the shock due to the same mechanism. Figure (9) shows the distribution of temperature of the electrons, and we see the above mentioned features along with a jump in temperature near the inlet. This jump is due to the characteristics based inlet boundary condition which ensures that the temperature at the inlet is picked based on the inlet value, i.e. 3900 K. In physical terms, it is like having the d.c.-arc heater from experiments sitting at the inlet.

Catalytic wall boundary conditions were used on the wall of the shell assuming that the wall was fully catalytic for the ions, meaning that all the ions that came towards the wall recombined with an electron to form a neutral atom. This would decrease the density of the ions near the shell and result in a thin sheath (see Poggie[15,16,17]) of electrons very close to the wall. However, even though we used the right catalytic boundary conditions, and we saw a decrease in density of ions close to the wall relative to a non-catalytic wall condition, we did not see a sheath of electrons close to the wall in our simulations. This is because the

thickness of the sheath is equal to the Debye length given by,

$$\lambda = \left[\frac{e^2 n_\infty}{K_b \epsilon_0}\left(\frac{1}{T_i} + \frac{1}{T_e}\right)\right]^{-1/2}, \tag{26}$$

and is equal to 10^{-7} m for this test case, but the smallest spacing of our mesh normal to the shell is 8 $\times 10^{-6}$m. Thus the thickness of the sheath of electrons is smaller than the smallest spacing near the wall and it is not possible to resolve it. This seems like the most probable reason why the sheath is not visible in these simulations and we hope to address this issue by further refining the mesh near the shell in our future work.

A numerical simulation in non-ionized Argon gas at the same test conditions as in the experiment was also carried out by solving the Navier-Stokes equations for a single species to compare the heat flux results with a multi-species plasma simulation with all the nonequlibrium chemistry. The results of heat transfer from a single species simulation are plotted on the same graph as a full multi-species simulation and the experimental data in Figure (10) and there is a big difference in heat flux from a single species Navier-Stokes simulation and a full multi-species plasma simulation with nonequilibrium chemistry. The plasma dynamic simulation results match the experimental data very well while Navier-Stokes simulations fail to capture the heat flux. The reason being that the heat transfer computation in the multi-species plasma simulations was done by adding the contributions from both Argon and the ion fluid. However, in the single species Navier-Stokes computation, heat transfer was only through the Argon gas. The expression for heat transfer is independent of density. It only depends on the gradient of temperature of the fluids near the wall and their viscosities. Another reason for the failure of a single species Navier-Stokes solution in capturing the heat flux correctly is that because of the thermo-chemical nonequilibrium processes included only in a full plasma dynamic simulations, the temperatures in a plasma dynamic simulations are different from the temperature in a single species Navier-Stokes equations where such processes are not simulated.

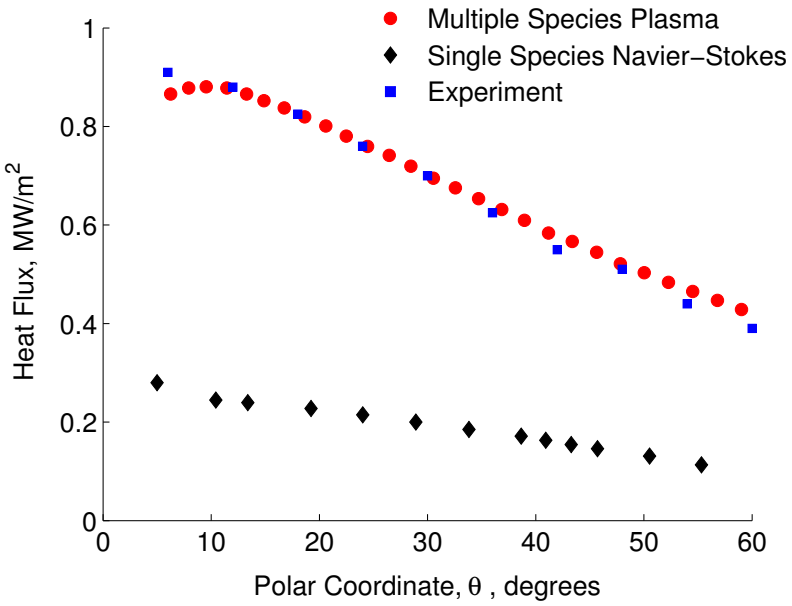

Figure 10. Comparison of numerical heat flux to the shell along the nose with experiments done at NASA Langley. The figure shows the importance of modeling all the species in an ionized gas over high speed vehicles to correctly capture the rate of heat transfer to the surface.

5. Conclusions

We have successfully verified and validated (with two initial test cases) a new formulation of the equations governing the dynamics of flows with multiple species in thermo-chemical nonequlibrium. The equations consist of a set of the Navier-Stokes equations for each species, augmented with source terms to account for thermo-chemical nonequilibrium chemistry coupled with Gauss's law from Maxwell's equations. The formulation includes the effects of local separation of charge in the flow. A numerical program which solves these equations has been developed in the computational suite, SU^2. Two different test cases have been simulated using this numerical tool and show excellent match with published data and computations. In the first case, the unsteady dynamics of the formation of plasma just ahead of a normal shock wave at Mach 15 is simulated, including the effects of local charge separation and, in the second case, the heat transfer from a supersonic stream of plasma to a solid body is numerically computed and compared with experiments done at NASA. The simulations clearly show the importance of including the effect of separation of charge in the flow and the importance of solving the full Navier-Stokes equations for each species in the plasma. The Mach number of the various species in the plasma varied by several orders of magnitude and SU^2 was able to capture the physics of all the species very well. The code will further be developed to simulate plasmas in air for dielectric barrier discharge for flow control applications and model heat transfer in hypersonic entry vehicles in different atmospheres.

6. Acknowledgements

Amrita K. Lonkar would like to acknowledge the support from the Stanford Graduate Fellowship.

References

[1]Chen, F. F., *Introduction to Plasma Physics and Controlled Fusion*, Plenum, 1984.

[2]Park, C., *Nonequilibrium hypersonic aerothermodynamics*, John Wiley and Sons Inc., 1990.

[3]Lee, J. H., "Basic Governing Equations for the Flight Regimes of Aeroassisted Orbital Transfer Vehicles," *Progress in Astronautics and Aeronautics: Thermal Design of Aeroassisted Orbital Transfer Vehicle*, Vol. 96, No. 19990066622, 1985, pp. 3–53.

[4]MacCormack, R. W., D'Ambrosio, D., D.Giordano, Lee, J. K., and Kim, T., "Plasmadynamic Simulations with Strong Shock Waves," *AIAA*, Vol. 27, No. 3921, 2011, pp. 194–204.

[5]Gokcen, T., "Computation of hypersonic low density flows with thermochemical non equilibrium," 1989.

[6]Hoffert, M. I. and Lien, H., "Quasi-One Dimensional Nonequilibrium Gas Dynamics of Partially Ionized Two-Temperature Argon," *The Physics of Fluids*, Vol. 10, 1967.

[7]Itikawa, Y., "Momentum-Transfer cross sections for electron collision with atoms and molecules," *Atomic Data and Nuclear Data Tables*, Vol. 14, 1974, pp. 1–10.

[8]Hirsch, C., *Numerical Computation of internal and external flows.Volume-2*, Wiley-Interscience, 1991.

[9]Roe, P. L., "Approximate Riemann Solvers, Parameter Vectors and Difference Schemes," *Royal Aircraaft Establishment, Bedford, United Kingdom*, 1981.

[10]Nowak, R. J. and Yuen, M. C., "Heat Transfer to a Hemispherical Body in a Supersonic Argon Plasma," *AIAA*, Vol. 11, No. 11, 1973, pp. 1463–1464.

[11]Jameson, A., "Solution of the Euler Equations for Two-Dimensional Transonic Flow by a Multigrid Method," Mae report no. 1613, Dept. of Mechanical and Aerospace Engineering, Princeton University, 1983.

[12]Jameson, A., "Solution of the Euler Equations by a Multigrid Method." *Applied Mathematics and Computation*, Vol. 13, 1983, pp. 327–356.

[13]Nakahashi, K., "FDM-FEM Zonal Approach for Computations of Compressible Viscous Flows," *Lecture Notes in Physics*, Vol. 264, Spring-Verlag, 1986, pp. 494–498.

[14]Nakahashi, K., "A Finite-Element Method on Prismatic Elements for the Three-Dimensional Navier-Stokes Equations," *Lecture Notes in Physics*, Vol. 264, Spring-Verlag, 1989, pp. 434–438.

[15]Poggie, J. and Sternberg, N., "Numerical Simulation of Electrode Sheaths in a Magnetized Plasma," *AIAA*, , No. 0359, 2003.

[16]Poggie, J., "Role of Charged Particle Inertia in Pulsed Electrical Discharge," *AIAA*, , No. 1195, 2010.

[17]Poggie, J., "High-Order Numerical Methods for Electrical Discharge Modeling," *AIAA*, , No. 4632, 2010.

7. Appendix

Table 4. Reaction Constants for ionization of Argon

s	C_s	T_s	η_s	θ_s	C_{K_s}	ζ_s	ϕ_s
Ar	10.12	T	1.5	135300	2.9×10^{22}	1.5	183100
Ar^+	10.12	T	1.5	135300	2.9×10^{22}	1.5	183100
e^-	22.59×10^4	T_e	1.5	135300	2.9×10^{22}	1.5	183100

Table 5. Physical properties of plasma in Argon

Quantity	Argon (Ar)	electron (e^-)	Argon ion (Ar^+)
Molecular Weight (M_s, kg/mol)	39.93	54.20×10^{-5}	$M_n - M_{e^-}$
Particle Mass (m_s, kg)	6.628×10^{-26}	9.108×10^{-31}	$m_n - m_{e^-}$
Particle Diameter (d_s, m)	4.0×10^{-10}	0	4.0×10^{-10}
Charge Number (Z_s)	0	-1	1